Morphological and microstructural characterization of an ancient Chola bronze statuette by neutron-based non-invasive techniques

Cantini, Francesco; Creange, Sara; Li, Yueer; van Eijck, Lambert; Kardjilov, Nikolay; Kabra, Saurabh; Grazzi, Francesco

DOI
10.1007/s12520-024-01948-z

Publication date
2024

Document Version
Final published version

Published in
Journal of Archaeological Science

Archaeological and Anthropological Sciences (2024) 16:45
https://doi.org/10.1007/s12520-024-01948-z

RESEARCH

Morphological and microstructural characterization of an ancient Chola bronze statuette by neutron-based non-invasive techniques

Francesco Cantini[1,2,3] · Sara Creange[4] · Yueer Li[5] · Lambert van Eijck[5] · Nikolay Kardjilov[6] · Saurabh Kabra[7] · Francesco Grazzi[2,3]

Received: 4 December 2023 / Accepted: 10 February 2024 / Published online: 28 February 2024

Abstract

The evolution of metallurgy is a fundamental aspect related to the knowledge of the technological level of ancient civilizations, for which the information was mostly part of an oral tradition. The ancient, preserved artefacts are the only keepers of this long gone knowledge. Most advanced non-invasive techniques provide us the key to access it. Neutron techniques are nowadays the only available approach for revealing, non-destructively and with good spatial resolution, the morphological and microstructural properties within the whole volume of densely composed artefacts such as bronze statues. Application of neutron methods allows us to learn about ancient artefact manufacturing methods and to study at a very detailed level the current conservation status in their different parts. As part of a research project dedicated to the study of ancient Asian bronzes led by the Rijksmuseum Metal Conservation Department, four statues from the Rijksmuseum Asian collection were analysed using non-invasive neutron techniques. In this work, we present the investigation of a South Indian bronze statuette depicting Shiva in the form of Chandrasekhara (AK-MAK-1291, c. 1000–1200 A.D.) by means of white beam tomography, energy-selective neutron imaging (performed on CONRAD-2 at HZB, DE, and on FISH at TU-Delft, NL), and neutron diffraction (on ENGIN-X at ISIS, UK). The application of neutron imaging revealed the inner structure of the statue and allowed us to investigate the conservation state and potential cracking on the surface and in the bulk, to understand the interconnection of the different sections of the statue, and to obtain clues about the manufacturing processes. These morphological and microstructural results were employed to guide neutron diffraction analyses that allowed us to precisely characterize compositional differences, the presence of dendrites and columnar growth peak structures related to casting. This work is a complete non-invasive analytical investigation on an archaeological bronze artefact, providing outstanding results: from a quantitative analysis of the composition and microstructure to an in-depth morphological analysis capable of unveiling details on the ancient casting methods of the statue.

Keywords Chola bronze statuette · Neutron techniques · Non-invasive technological study of ancient casting methods

✉ Francesco Cantini
f.cantini@unifi.it

[1] Università degli Studi di Firenze (UNIFI), Dipartimento di Fisica, Sesto Fiorentino, Italy

[2] Consiglio Nazionale delle Ricerche, Istituto di Fisica Applicata Nello Carrara (CNR-IFAC), Sesto Fiorentino, Italy

[3] Istituto Nazionale di Fisica Nucleare, Laboratorio di Tecniche Nucleari per i Beni Culturali (INFN-Labec), Sesto Fiorentino, Italy

[4] Rijksmuseum Conservation and Science Department, Amsterdam, Netherlands

[5] Technische Universiteit Delft (TU-Delft), Fac. Applied Sciences, Dep. RST/NPM2, Delft, Netherlands

[6] Helmholtz-Zentrum Berlin (HZB), Wannsee, Germany

[7] ISIS Neutron and Muon Facility, STFC-UKRI, Rutherford-Appleton Laboratory, Harwell Campus, Didcot OX11 0QX, UK

Introduction

The study and the preservation of historical artefacts are grounded upon the intimate knowledge of the constituent materials and the understanding of their manufacturing methods. It is essential to have diagnostic tools capable of providing the highest amount of information with a minimum of invasiveness.

The Rijksmuseum Metal Conservation Department initiated the technical study of a South Indian bronze *Chandrasekhara* ('the moon-crested one', hereafter referred to as Shiva, AK-MAK-1291, c. 1000–1200 A.D.) along with three other bronzes from India and Southeast Asia. The date, estimated on stylistic grounds, falls within the Chola Dynasty in South India (Srinivasan 2006). During this period, a bronze casting industry developed in the region of the Kaveri River, specializing in solid-cast bronzes up to several metres tall, of a scale and quality unmatched in the rest of the world (Dehejia 2021). Casting was closely linked with religious ritual, and the methods were to a certain extent codified in religious texts and passed down through generations of bronze-casting families. Descendants of the Chola casters still produce bronzes largely following the ancient methods (Levy, et al. 2007).

This provides a unique opportunity to examine features found in ancient statues with reference to current local casting practice and ritual casting described in ancient texts.

The Shiva (Fig. 1) is a four-armed figure standing on a pedestal and backed by a flaming halo (Fig. 1); it is owned by the Royal Society of the Friends of Asian Art (VVAK) and housed in the Rijksmuseum in Amsterdam. The statuette at 40 cm and 4.9 kg is not particularly large for a Chola bronze and was made by means of the direct lost wax casting technique. According to initial visual assessments and knowledge of current casting practice in South India (Levy, et al. 2007), it is assumed the Shiva could be cast in three separate parts that are then mechanically joined: the figure, the pedestal which consists of a rectangular base topped with a circular double lotus flower, and a flaming halo inserted into brackets at the side of the pedestal. No bulk analysis of the alloy composition had been performed prior to this work; the statue was believed to have comparable composition to typologically similar sculptures, with an alloy of nearly pure copper (Craddock & Hook 2007; Werner 1972). A different alloy is believed to have been used for the arched structure, the so-called halo. The Shiva figurine is decorated with bas-relief jewellery including bracelets, necklaces, earrings, and a ribbon. The necklace ends with a pendant which, under visual inspection, appears very dark and is suspected to be a precious metal.

Preliminary surface analysis by X-ray Fluorescence (XRF) is difficult because of the presence of corrosion and soil. The surface appears mainly light green in colour, probably due to the presence of anhydrous copper sulphate, copper carbonates, and copper-based silicate concretions. Below the pedestal is possible to observe azurite, malachite, and cuprite. Based on qualitative XRF measurements (Olympus handheld and comparisons with other published Chola bronzes) (Craddock & Hook 2007; Srinivasan 1999), the main alloy is supposed to be mostly copper with the addition of tin and lead.

Common X-ray non-invasive diagnostic techniques for characterizing metals, such as X-ray diffraction and imaging, do not allow microstructural analysis and do not possess high power penetration in thick materials consisting of heavy elements. For this reason, optical microscopy techniques

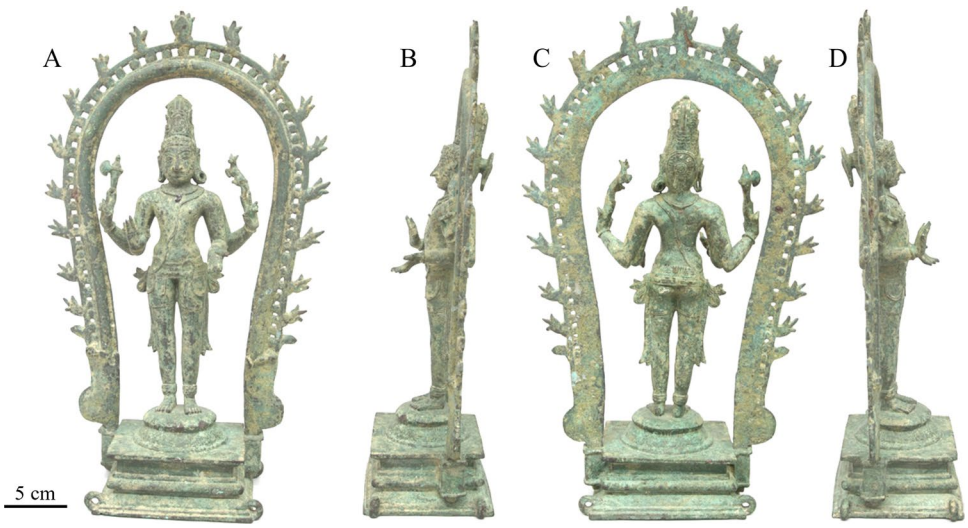

Fig. 1 The Shiva bronze statuette (AK-MAK-1291). Views of the artefact: front (**A**), left side (**B**), verso (**C**), and right side (**D**)

have traditionally been used—e.g., metallography—which are however highly invasive, requiring a substantial withdrawal of material from the sample. The use of neutron as an investigation probe for metallic artefacts has made it possible to have non-invasive microstructural analytical techniques. Unlike X-rays, the use of neutron allows to discern between metals with similar atomic numbers, because of large differences in the cross-section among metals and a good penetration into materials, even with a thickness of several centimetres.

The quality and quantity of information that can be achieved with neutron diffraction and imaging techniques can provide, further supported by the interdisciplinary contribution in data interpretation, information ranging from structural and microstructural description to the analysis of the state of conservation of the artefact up to the technological process involved in its manufacturing.

The thorough characterization of this statue required a multianalytical approach, organized in three different experimental campaigns (Neutron Imaging, Neutron Diffraction, and Neutron Activation Analysis) at three international facilities (2016, Helmholtz Zentrum Berlin, DE; 2019, ISIS Neutron and Muon Source, UK; 2022, Reactor Institute TU Delft, Delft, NL).

Neutron Imaging (NI) analysis allows for morphological and microstructural results that reveal clues related to the casting process and the relationship among the various constituent parts of the statue (the pedestal, the halo, and the Shiva figurine). Both White Beam Neutron Tomography (WB-NT) and Energy-Selective Neutron Radiography (ES-NR) were exploited to achieve a complete morphological characterization as well as information about the casting techniques involved in the manufacturing of this artefact. Time-of-Flight-Neutron Diffraction analysis (ToF-ND) driven by Neutron Imaging (NI) results was used primarily for the alloy characterization and to study precise areas of the statue aiming to better understand some morphological features highlighted by tomography reconstruction. Further insights, which became necessary following the data analysis of the first two experimental campaigns, were achieved by means of thermal WB-NT followed by Neutron Activation Analysis (NAA).

The goal of this work was to analyse the phase and elemental composition, to investigate the presence of specific mineral phases related to corrosionto investigate the structural stability, to verify that the sculpture is a solid cast, to determine the number of separately cast parts, and to investigate what type of joint was used between the various parts (e.g., mechanical joint or by applying soldering medium). Moreover, one of our goals was to exploit morphological and microstructural analysis to provide clues about the casting process such as the orientation of the mould during casting.

Methods

To be able to answer the afore-mentioned questions, several neutron methods were applied. NI allows to investigate the interior of bulk metals in a completely non-invasive way without any pre-treatment of the statuette. Likewise, ToF-ND and NAA are both non-invasive methods and can be used to investigate the interior of such bulk objects.

Neutron imaging (NI)

White Beam Neutron Tomography (WB-NT) of the entire statue was performed using the cold neutron beamline CONRAD-2 (Kardjilov, et al. 2014). At the same beamline, Energy-Selective Neutron Radiography (ES-NR) was also performed to visualize the crystallinity variations over the statue. The cold WB-NT was later complemented with thermal WB-NT at the FISH beamline (Zhou, et al. 2018).

WB-NT yields the three-dimensional entire structure of the statue, very similar to CT scans used in hospitals. The 3D computer model can then be used to explore the interior of the object through the variations in grey value of the images in (virtual) computed slicing of the 3D model in any direction. With a sub-millimetre spatial resolution, it renders microstructural details of the bronze casting and is an essential tool for investigating the manufacturing methods and determining the conservation state. In the case of bronze; the thickness of the metal; the presence of fractures, gaps, and defects; and the presence of porosity can be investigated (Lehmann et al. 2010; Grazzi et al. 2018; Schulz et al. 2024; Salvemini et al. 2023).

Cold neutron tomography

The entire statue was investigated with NT using the cold neutron beamline CONRAD-2 of the BERII 10-MW research reactor at Helmholtz Zentrum Berlin (HZB) in Berlin, Germany. The instrumental resolution was set by using a scintillator screen of 200 μm thickness and a pinhole that sets the beam divergence to L/D = 250, yielding a neutron flux of 10^7 cm^{-2} s^{-1}. Because the statue is larger than the neutron beam Field of View (FoV), the tomography was performed by collecting transmission images for 500 angular positions of the portion in the neutron beam, for two vertical positions of the statue. We also acquired 10 Dark Current (DC) images and 10 Open Beam (OB) images. In order to remove high-intensity pixels generated by scintillator defect or by gamma particle, the whole data set was pre-treated exploiting Remove Outliers filter by ImageJ software (Rasband 2007; Rueden et al. 2017). DC images were subtracted from both the raw radiographic stack and the

OB image, to minimise thermal noise contribution. Then, the stack was divided with respect to the median value of the OB images to normalise neutron beam intensity fluctuation. The two resulting projection data sets were stitched together, and the 3D model was reconstructed using the Filtered Back Projection algorithm (FBP) of the Octopus Reconstruction software package (Dierick, et al. 2004). During the reconstruction routine, a polynomial ring filter was applied as well as the rotation axis correction and tilt correction. Notwithstanding the data reduction and filtering procedure, the final slices are affected by some reconstruction artefacts. More details are reported in the Supplementary material S1. Nonetheless, these types of reconstruction artefacts are easily recognizable, and it was therefore possible to carry out consciously the morphological and microstructural analysis of the imaging data. The 3D volume reconstruction, segmentation, and rendering were obtained using 3D Slicer 4.11 (Fedorov, et al. 2012).

Thermal neutron tomography

Additional NT was performed at the FISH beam line of the research reactor at TU Delft, the Netherlands (Zhou, et al. 2018). Highly attenuating materials are visualized in higher detail by thermal neutrons than cold neutrons, as the beam hardening artefacts are less severe due to the spectral properties of the thermal neutron beamline. The stacked neutron guide of FISH provides a thermal neutron beam with a wavelength band centered on 1.59 Å (van Well, et al. 1991), c.f. the cold spectrum of CONRAD. In addition, the setup has slightly better L/D ratios of 325 and 277 in horizontal and vertical directions respectively, yielding a slightly improved spatial resolution of the reconstructed 3D model. Because of the limited Field of View (FoV) of the beamline, measurement of the shoulder and neck volume was performed using 3 horizontal positions of the statue in the beam, extending the FoV from 80×140 mm^2 to 210×140 mm^2, including 10 mm side by side superimposition area to correctly perform stitching. For the experiment, we used a 200-µm-thick ^{6}LiF/ZnS scintillator yielding a 3D spatial resolution of approximately 400 µm. The data were converted to a 3D model using the same software as for the CONRAD data set.

Energy-selective neutron radiography scan

The wide neutron energy range of the CONRAD-2 beamline allows to inspect the microstructural properties of the statue. Energy-selective radiography is based on the acquisition of a series of neutron transmission images, where each image is generated by transmitted monochromatic neutron beam. This condition is achieved by using a double crystal monochromator, able to select a specific wavelength by maintaining the beam parallel to the pre-filtered conditions (Salvemini & Grazzi 2012; Josic, et al. 2011). By performing a wavelength radiography scan, the contrast of the transmission image in crystalline areas of the sample changes due to the so-called Bragg cut-off. In fact, for each crystalline phase in the bronze, depending on its lattice arrangement, there are characteristic neutron wavelengths at which the beam transmission suddenly increases for a tiny increase of the wavelength. From the analysis of the series of transmission images, one can infer useful details about phase distribution and relative concentration. Moreover, if there are discrepancies in the crystallographic domain microstructure with respect to the standard features of a polycrystalline material (homogeneous composition, large-size grains, isotropic orientation distribution, regular rounded shape), the Bragg-edge imaging set will provide specific different attenuation coefficients. The data set of 31 transmission images was collected at wavelength steps of 0.05 Å from 3.0 to 4.5 Å. The experimental setup parameters for all neutron techniques used in this work are described below in Table 1.

Neutron diffraction (ND)

ND allows studying the atomic scale crystalline structure of the bulk of the statue, non-invasively. Rietveld refinement allows to obtain quantitative phase analysis and then the relative concentration of the different structural arrangement of the sample components. Moreover, by performing ToF-ND on the ENGIN-X beamline of the ISIS Neutron and Muon Source, Didcot, UK, and exploiting the high resolution collimation devices, such crystalline structures can be determined for specifically selected sub-volumes within the statue. Rietveld analysis of the ToF-ND data makes it possible to obtain information of the binary concentration of copper and tin in bronze (single phase alloy for Sn wt% less than 10%), lead concentration, presence and amount of non-metal mineralization phases, presence and distribution of residual strain, intra-granular microstructural strain, domain size, and grain orientation texture index. Experimental data were collected for a selection of 21 sub-volumes of $2 \times 2 \times 2$ mm^2, using a neutron wavelength band of 0.5–6 Å and two detector banks positioned at $\pm 90°$ (2θ) scattering angle. Data analysis was carried out exploiting Rietveld refinement method using GSAS software (Toby 2001; Von Dreele & Larson 2004) that allows for phase characterization. Quantitative phase analysis and elemental composition were obtained exploiting of calibration curves published by Grazzi et al. (Grazzi, et al. 2010).

Table 1 Neutron imaging experimental configuration parameter for the three experimental sessions. *Energy-selective scan requires static sample that can be placed much closer to the detector, increasing the resolution.

Neutron Imaging experimental configuration			
Parameter	White beam neutron tomography @ CONRAD-2	Energy-selective scan @ CONRAD-2	White beam neutron tomography @ FISH
Neutron beam peak value	~0.4 nm	~0.4 nm	0.159 nm
Field of view	300 × 300 mm^2	300×300 mm^2	240×140 mm^2
Scintillator	^{6}LiF/ZnS, t = 200 µm	^{6}LiF/ZnS, t = 200 µm	^{6}LiF/ZnS, t = 200 µm
Spatial resolution	~480 µm	~230 µm*	~400 µm
L/D	250	250	H = 325; V = 277
#Projections/radiograms	500	31	500
Acquisition time	15 s	200 s	15 s
Rotation axis to scintillator distance	15 cm	6 cm	15 cm
Beam modifier		DCM—Double Crystal Monochromator ($\Delta\lambda/\lambda$=3%)	
Wavelength interval	3.0–15 Å	3.0–4.5 Å	0.7–4.1 Å
Wavelength step		0.05 Å	

Neutron activation analysis (NAA)

NAA was used to non-destructively determine the elemental composition of the pendant, below the corrosion layer. It is based on spectroscopy of gamma photons emitted by radioactive isotopes (Greenberg, et al. 2011). The radioactivity is generated during neutron irradiation and decays through photon emission with isotope-specific energy and time constant. By analysing the gamma spectrum, a quantitative elemental composition is determined, if the attenuation of neutrons and gamma photons inside the object is accounted for.

The neutron irradiation was performed at the FISH beamline, which provides a neutron flux density of 6.5×10^6 n cm^{-2} s^{-1}. Gamma spectroscopy was done using a detector system consisting of a HPGe crystal of 26.9% relative efficiency and a DSPEC multichannel analyser providing 8192 channel spectra with energy ranging from 200 to 3600 keV. The Shiva's chest area was irradiated at the FISH beamline for 22.5 h to ensure that sufficient numbers of Au and Ag atoms (potential components of the pendant) would be activated to obtain a measurement uncertainty less than 1%. Activation gamma spectra were measured 6 days after irradiation; the distance from the detector surface to the pendant surface was 3 cm.

Results and discussions

In this section, the results will be presented and discussed; they are not organized according to the used analytical techniques, but according to the type of information they can provide: the morphological/microstructural study of the artefact, the composition of the alloy, and the 'reconstruction' of the manufacturing method used to produce the statuette.

General morphological description

The WB-NT reconstruction confirms that both the figurine and the halo are solid cast. The pedestal is revealed to be a complex hollow structure (Fig. 2). The housing for the halo pins on the side of the square base allows for a mechanical connection: the use of a small amount of hard solder material (Giumlia-Mair 2012; Azéma et al. 2017) for this joint cannot be completely ruled out, as there are some points of interconnection between the pins and the wall of the brackets. The contact points in some cases can be identified as earthy concretions showing a lower grey value than the metal, while in specific points, the presence of material sharing the same grey tone as the metal is evident. Mineralization phases are certainly present in the interstices left in the pin housing (see Supplementary material S2).

Despite some reconstruction artefacts, such as shadowing effects, the alloy appears homogeneous for the pedestal, the Shiva figurine, and the halo; in fact, the three sections of the statue have relatively similar composition as reported by the ToF-ND compositional analysis (see the 'Alloy characterization' section) (Fig. 9 and Table 2). In the Shiva figurine, widespread ubiquitous porosity can be observed (Fig. 3): the pores have a rather varied size distribution ranging in size of several hundred micrometres (500–1000 µm Ø). Considering the spatial resolution limit for cold NT of 480 µm, it seems that neither the halo nor the pedestal is affected by strong porosity.

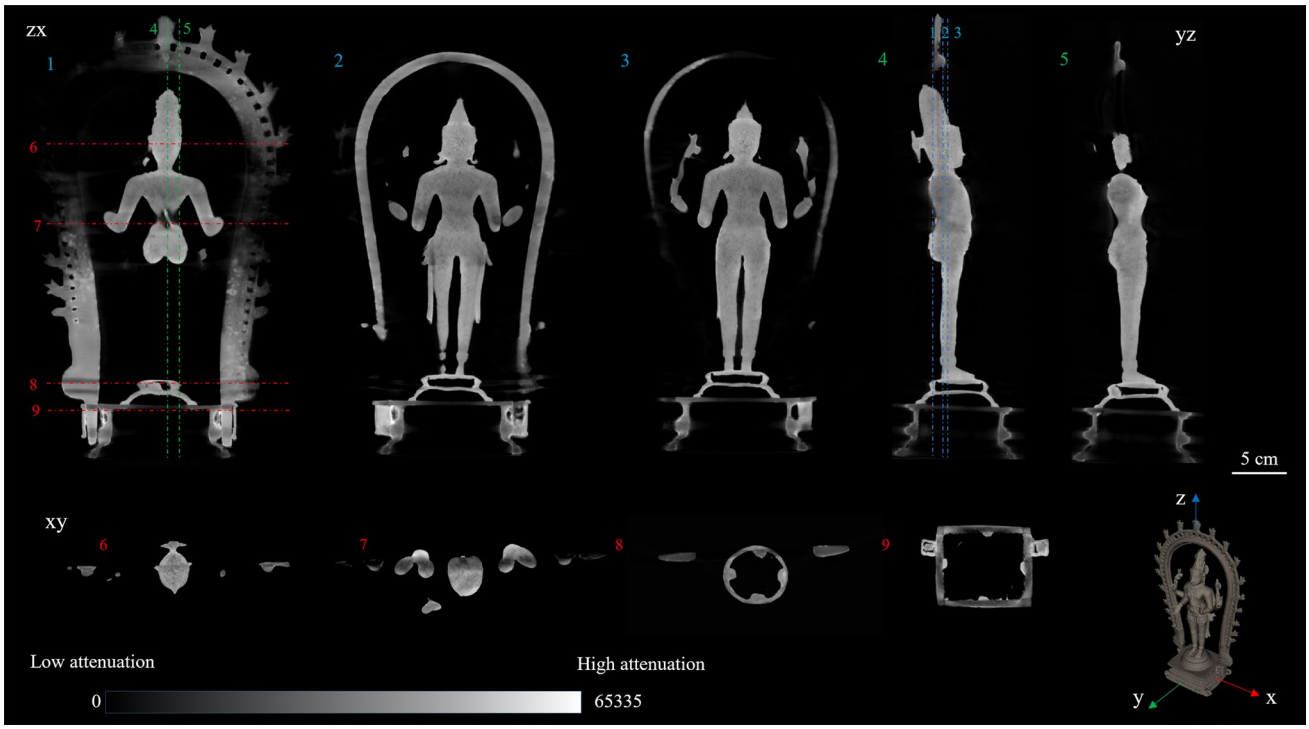

Fig. 2 Shiva (AK-MAK-1291). Neutron tomography projections. Normal slices (*zx*); sagittal slices (*yz*); axial slices (*xy*)

The statuette is in a good state of conservation considering that it is an archaeological artefact, both from a structural point of view and from the corrosion of the alloy. In the whole artefact, there are no significant fractures except for a single 16-mm-long crack inside the belly of the statue, which is likely due to shrinkage of the metal during cooling and does not seem to affect the structural stability of the object.

Hydrogen is present in several mineralization phases and strongly interacts with the neutron, resulting particularly bright in the tomographic images. This allows us to obtain both surface and bulk mapping of the corroded areas. As can be seen in Fig. 3, the presence of mineralized phases is limited to the surface and, in particular, associated with residues of concretions trapped in the undercuts, or in the areas of the figurine richer in finely decorated details.

The same situation can be observed for the pedestal, where the most attenuating phases are identified in the junction between the halo pins and the brackets (for more detailed images, please refer to Supplementary material S2). ToF-ND phase analysis allowed us to identify and quantify some of the main copper alloy alteration products (see Fig. 4 for the inspection locations of ToF-ND analysis). Cuprite is present in low concentrations exceeding 1 wt% only in two analysed measurement areas; nantokite, which can be an indication of active corrosion, is present in only four areas of the 21 investigated ranging from 0.1 to 0.9 wt%. Other phases suggesting active corrosion such as paratacamite and atacamite were not found. Consequently, it seems that the bulk of the statue is not affected by active corrosion.

Chalcocite has not been identified: the undetectability of this phase does not exclude its presence in quantities below the detection limit (0.1 wt%) for the ToF-ND analysis.

The pedestal

As described in the 'Introduction' section, the pedestal is a hollow form consisting of a square base surmounted by a semi-dome structure representing the lotus flower, from which Shiva emerges. There are many examples of statuettes of the similar typology, and many are described in the literature from an archaeological/artistic point of view, but technical studies are rare, especially of the pedestals (some known examples are described in (Craddock & Hook 2007) and (Dehejia 2021). Often the pedestal is described as a single piece, either mechanically mounted or cast as one with the figurine of the deity. The tomographic reconstruction highlighted some discontinuities at the height of the upper level of the square base from which 'the lotus flower' originates (Fig. 5); these are thickenings of a few millimetres that follow the circumference of the base of the lotus flower. However, this observation is not sufficient to hypothesize that the two parts were cast separately and then assembled; indeed, the discontinuities could be attributed to a joint created during the preparation of the wax model of the statuette. The

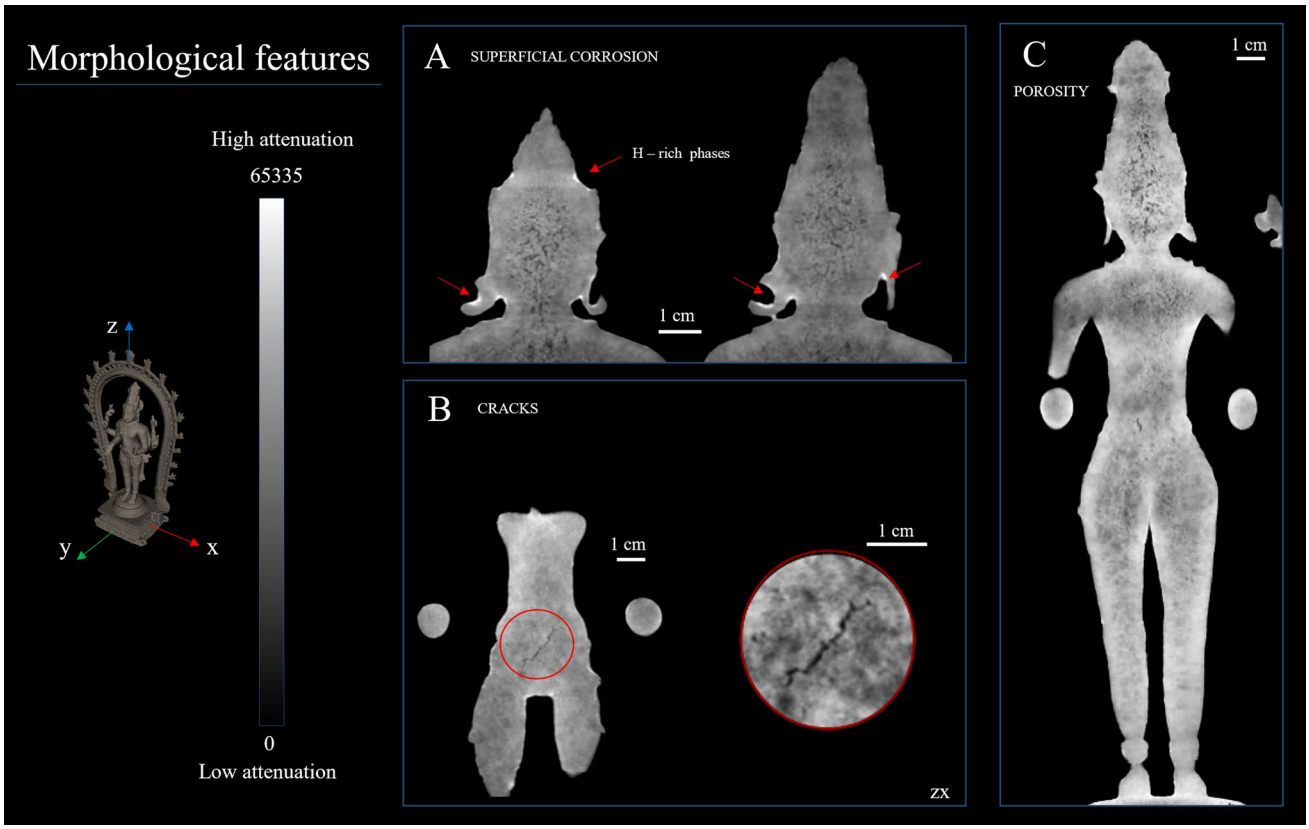

Fig. 3 Shiva (AK-MAK-1291). Neutron tomography normal slices of the Shiva figurine body showing morphological features: **A** close-up details of high attenuating phases, rich in hydrogen, thickening in the superficial interstices and in the undercuts of the earrings; **B** a cavity, which can be interpreted as an internal fracture or a shrinkage void, present in the belly of the figurine; **C** porosity ubiquitously present in Shiva's body. Gases are present within the mould before casting and furthermore develop during heating. Often, the gases are able to escape through vents in the mould; otherwise, they are absorbed into the mould material or trapped in the bulk of the metal, resulting in porosity

protrusions of wax inside the pedestal, if not removed, could have been faithfully transferred to the mould and finally to the cast bronze (wax on wax joint).

However, as seen in Figs. 5, 6, and 7, the square base has four inward extensions directly underneath the plane supporting the lotus pedestal. The sagittal and normal sections show that these supports do not always connect perfectly with the semi-dome structure of the lotus flower but appear to directly support the top plate of the square base (Fig. 7) (see also the pedestal assembly hypothesis in Supplementary material S3, Fig. S6–S8). This could support the hypothesis that the square base was cast independently from the lotus flower which could instead have been cast as a whole with the underlying plate acting as a lid for the underlying base. The two parts could have been joined by welding, and the lid with the lotus flower could have rested perfectly on the four supports. In support of this hypothesis, there are at least four examples of statuettes of the Chola period, in the collection of the Thanjavur Museum which do not have a square base but have the lotus flower connected directly to a rectangular plate (Dehejia 2021). Other examples of a lotus flower cast separately from a square base can be found as well (Slaczka, et al. 2019; Dehejia 2021).

WB-NT also allowed us to study the connection system between the Shiva figurine and the pedestal. The feet of the Shiva figurine end in a round flat structure which serves as a base. The statue and the circular footplate were cast together; indeed, no solder lines are visible here. The round footplate has a finer and more compact crystalline grain, probably due to the intense cold mechanical work undergone to fit the housing into the base.

To confirm that this footplate was cast together with Shiva, the microstructure at the interface between the foot and the round plate was observed. In Fig. 6A and B, two details of the normal section of the left foot are shown: the first image is a tomographic projection, and the second a 3D reconstruction. We observe the presence of two phases: the darker one can be attributed to dendrites with higher tin content. These dendritic structures are more than 500 µm

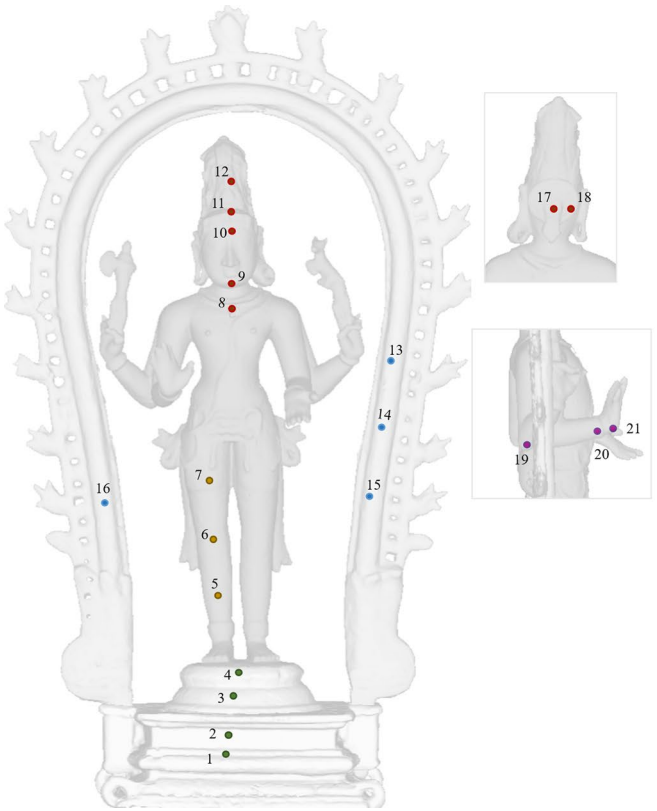

Statuette section	SAMPLE	Cuprite (wt %)	*Err.*	Nantokite (wt %)	*Err.*
HALO	16	0.2	*0.2*	/	/
	15	/	/	/	/
	14	/	/	/	/
	13	0.2	*0.1*	/	/
RIGHT ARM	21	0.2	*0.1*	/	/
	20	/	/	/	/
	19	/	/	/	/
HEAD	18	0.2	*0.2*	/	/
	17	/	/	0.4	*0.2*
	12	0.2	*0.1*	/	/
	11	0.2	*0.2*	0.1	*0.1*
	10	/	/	/	/
	9	0.3	*0.2*	/	/
	8	0.4	*0.2*	/	/
RIGHT LEG	7	/	/	/	/
	6	1.5	*0.4*	/	/
	5	1.2	*0.3*	0.2	*0.2*
BASEMENT	4	0.3	*0.1*	/	/
	3	/	/	/	/
	2	1.3	*0.3*	0.9	*0.2*
	1	0.4	*0.1*	/	/

Fig. 4 ToF-ND mineralization phase analysis. The numbered measuring points are depicted on the 3D visualization of the reconstruction model. The concentration of each phase is reported in %wt

in length on average and up to 2 mm across the interface extending from the foot to the base.

The solidification process of the molten alloy begins in contact with the colder walls of the mould, where a thin layer of crystals is formed, while the dendritic branches, richer in copper (the first component to solidify), propagate inwards. Subsequently, the Sn-rich branches will grow as last elements, on the dendritic structures of the first solidified volume (Scott 1991). The presence of dendrites across the interface supports the hypothesis that the footplate and feet were cast together rather than soldered. Moreover, the size of these microstructural features suggests that the cooling of the melt was slow enough to allow the formation of elongated dendritic like crystals hundreds of micrometres in size.

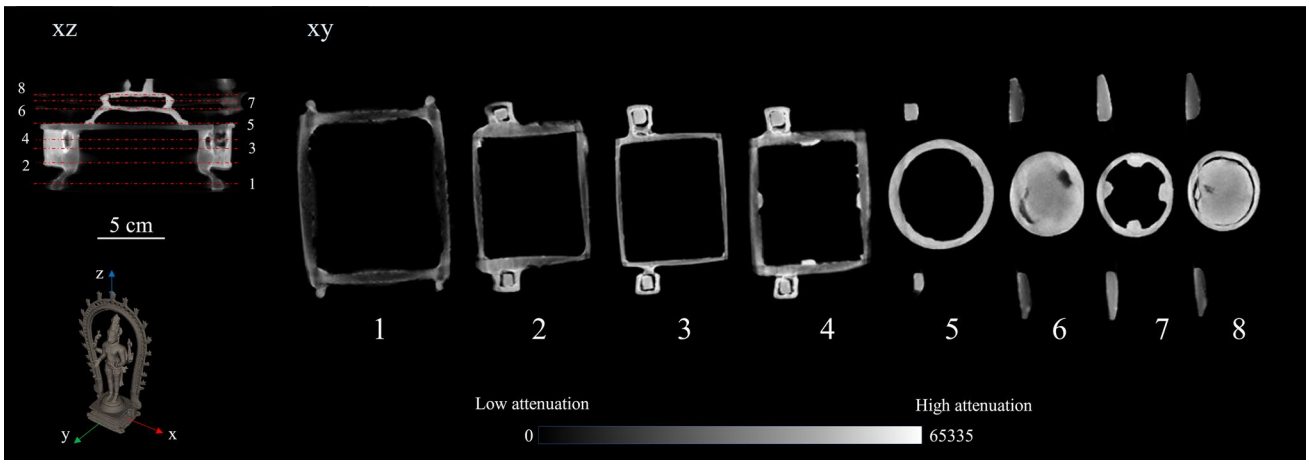

Fig. 5 Shiva (AK-MAK-1291). Pedestal. Neutron tomography. Axial (*xy*) projections

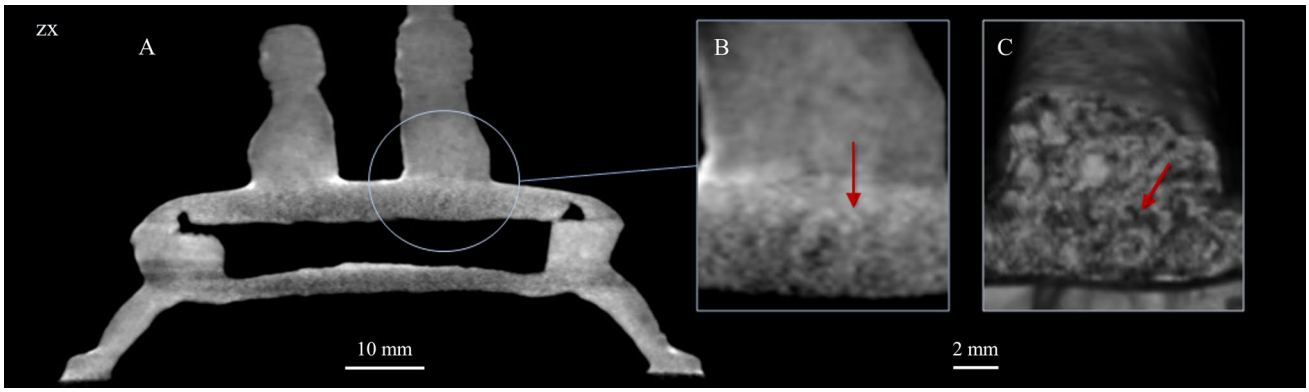

Fig. 6 Shiva (AK-MAK-1291)—pedestal details. **A** Neutron tomography normal slice of the statuette pedestal: the connection between the left foot and the round plate base is shown in detail in the close-up magnification in **B** and in **C** exploiting the three-dimensional model reconstruction. This close-up detail shows some dendrites that cross the round plate ending in the feet of the statue

The footplate, as seen in the axial projections in Fig. 6 or in detail in Fig. 7 (see also Fig. S9 in Supplementary material S3), rests on the four supports within the lotus flower. The assembly appears to have occurred mechanically by placing the figurine on supports within the flower and then by cold hammering to allow part of the edge to be folded back stabilizing the figurine to the pedestal (Craddock & Hook 2007). This method is a common practice in modern-day South Indian workshops.

In Fig. 8, we show the 3D segmentation of the three sections of the statuette and a possible representation of the assembly process.

Alloy characterization

In order to characterize the different portions of the artefact, looking for confirmation of what the WB-NT data suggest, neutron diffraction measurements were performed at multiple locations within the statuette, each location with a gauge volume of 5 mm × 2 mm × 2 mm.

Starting from an accurate determination of the lattice parameter of the face-centered cubic (FCC) copper alloy crystalline structure (alpha phase), it was possible to obtain the quantitative analysis of the alloy. In fact, bronze is a substitutional alloy with tin replacing some of the copper

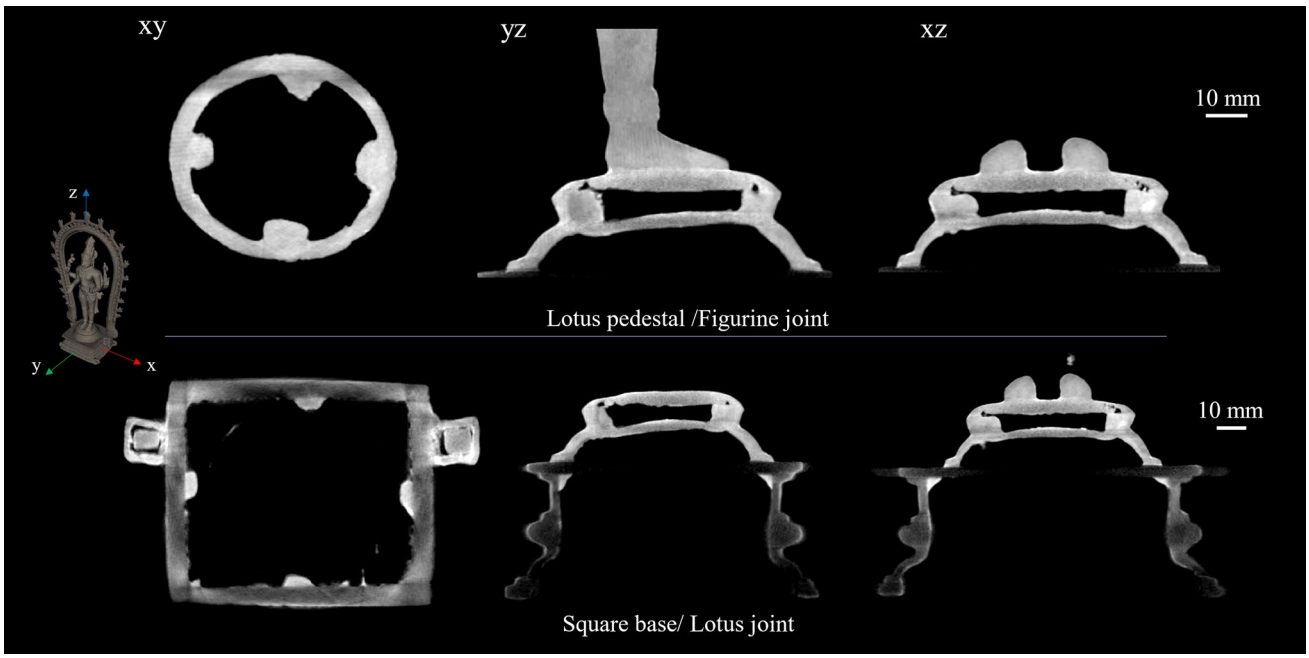

Fig. 7 Shiva (AK-MAK-1291)—pedestal joint details

atoms, and the lattice parameter of the alloy increases as a function of tin amount with respect to the pure copper value (3.6147 Å). The tin concentration of each sample was estimated by calculating the equivalent tin content as a function of lattice parameter. The equivalent binary Cu-Sn alloy composition was determined using the calibration curves published by Grazzi et al. (Grazzi, et al. 2010).

The results of the ToF-ND analyses are summarized in Fig. 9 and Table 2. The bronze alloy of the entire artefact is characterized by a low tin content between 2.4 and 4.6 wt% and by a lead concentration that varies widely from 2.9 to 12 wt%.

Since lead is not a copper alloying agent (miscibility of 0.1 wt %) and because it is the last element to solidify in a Cu-Sn and Pb system, it is forced to occupy intergrain positions left by the solidification of the Cu-Sn alloy. Therefore, lead is present in isolated spheroidal accumulations inhomogeneously distributed within the cast metal. Furthermore, its inhomogeneity may also depend on the preparation of the alloy in the crucible (Cantini, et al. 2023; Oudbashi, et al. 2020; Hughes, et al. 1982). For this reason, the various portions of the statue were compared, mainly considering the differences in tin concentration, to later evaluate the differences in lead content.

The halo, certainly cast separately, has an alloy with an average equivalent tin content of 4.6 wt%. The base and the Shiva figurine have very similar alloys (Tables 2 and 3). It is interesting to note that the base has an average Pb content of 3.3 wt%, lower than the other sections of the statuette. This could be attributed to a conscious choice to use a more fluid alloy with a lower melting point to carry out the solid cast: with these characteristics, the alloy could have finely filled the details of the moulds of the most valuable portions of the artefact: Shiva figurine and its flaming halo.

The pendant

The figurine of Shiva wears a necklace with a small pendant which, according to visual inspection, could be made of silver (now tarnished) possibly alloyed with gold (Fig.). From the tomographic images, this decorative element stands out with a very high attenuation coefficient (the grey value is 3 times the value of the body) confirming such hypothesis since both silver and gold have a high neutron absorption cross-section (Ag $\sigma_{scatt} = 5$ barn; $\sigma_{abs} = 63$ barn*; Au* $\sigma_{scatt} = 8$ barn; $\sigma_{abs} = 99$ barn).

This assumption is supported by the neutron diffraction analysis, which confirms that its main constituent is Ag or Au (lattice parameter compatible with Ag–Cu or Au-Cu alloy). However, the diffraction method alone, based on lattice parameter determination as discriminating factor, was not sufficient to univocally discern the composition. By performing NAA, the elemental composition of the pendant has been determined, yielding the Au and Ag concentration. The composition of the pendant has been determined, taking into account the inhomogeneity of the neutron beam and a correction for neutron self-shielding and gamma self-attenuation (Greenberg, et al. 2011) by simplifying the shape

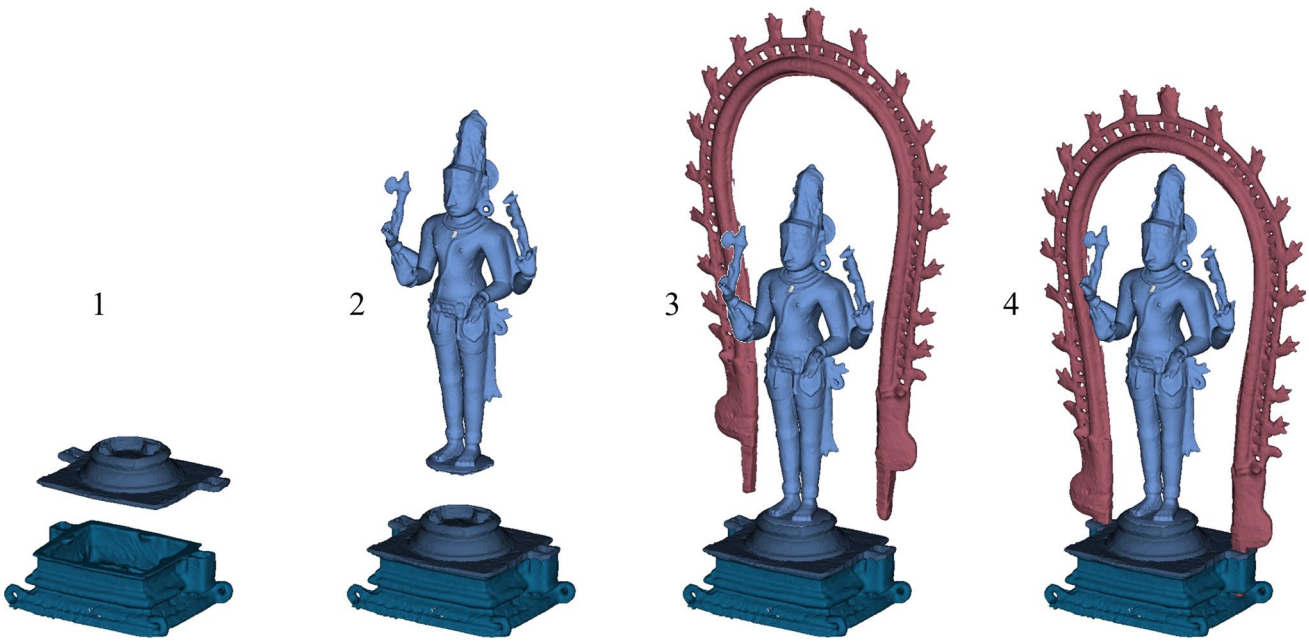

Fig. 8 Shiva statuette assembly of the presumed independently cast portions. **1** Hard soldering; **2** mechanical joint; **3** mechanical joint and/or hard soldering

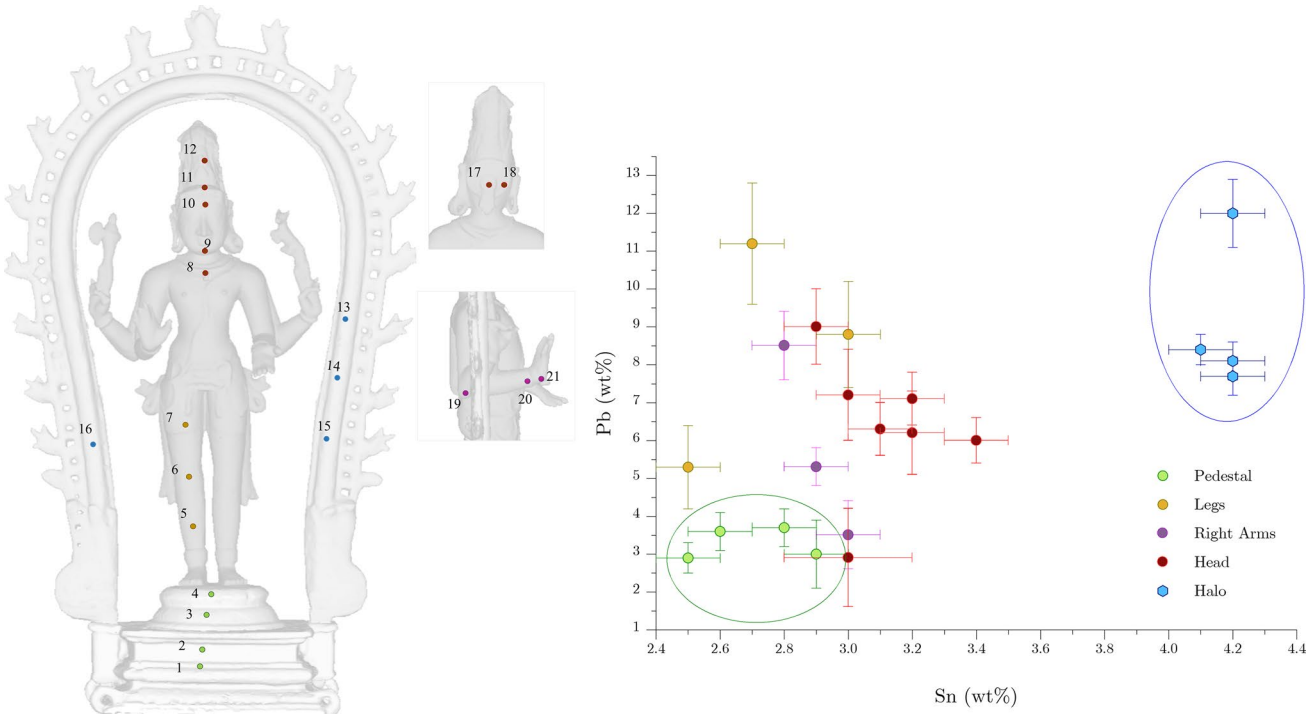

Fig. 9 ToF-ND alloy composition result. On the left of the figure, the measurement area positions are shown; on the right of the diagram, the distribution of the lead vs tin content (wt%) is reported (for more details, see Supplementary material S4)

Table 2 ToF-ND. Concentration (% wt) of the main elements present in the alloy as derived from Rietveld refinement. The column on the right records the weight percentage content of the equivalent tin in monophasic binary alloy with copper, for each sample

Measurement area	Sample	Cu (wt%)	Er	Sn (wt%)	Er	Pb (wt%)	Er	Sn (wt%) Binary	Er
Pedestal	1	93.8	*0.1*	2.6	*0.1*	3.6	*0.5*	2.7	*0.1*
	2	94.1	*0.1*	2.9	*0.1*	3	*0.9*	3.0	*0.1*
	3	93.5	*0.1*	2.8	*0.1*	3.7	*0.5*	2.9	*0.1*
	4	94.6	*0.1*	2.5	*0.1*	2.9	*0.4*	2.6	*0.1*
Right leg	5	88.2	*0.1*	3	*0.1*	8.8	*1.4*	3.3	*0.1*
	6	92.2	*0.1*	2.5	*0.1*	5.3	*1.1*	2.6	*0.1*
	7	86.1	*0.1*	2.7	*0.1*	11.2	*1.6*	3.0	*0.1*
Head	8	94.1	*0.2*	3	*0.2*	2.9	*1.3*	3.1	*0.2*
	9	90.6	*0.1*	3.1	*0.1*	6.3	*0.7*	3.3	*0.1*
	10	90.6	*0.1*	3.4	*0.1*	6	*0.6*	3.6	*0.1*
	11	89.8	*0.1*	3	*0.1*	7.2	*1.2*	3.2	*0.1*
	12	89.7	*0.1*	3.2	*0.1*	7.1	*0.7*	3.4	*0.1*
Halo	13	88.1	*0.1*	4.2	*0.1*	7.7	*0.5*	4.6	*0.1*
	14	87.7	*0.1*	4.2	*0.1*	8.1	*0.5*	4.6	*0.1*
	15	87.5	*0.1*	4.1	*0.1*	8.4	*0.4*	4.5	*0.1*
	16	83.8	*0.1*	4.2	*0.1*	12	*0.9*	4.8	*0.1*
Head (flower, nape)	17	90.6	*0.1*	3.2	*0.1*	6.2	*1.1*	3.4	*0.1*
	18	88.1	*0.1*	2.9	*0.1*	9	*1*	3.2	*0.1*
Right arm	19	88.7	*0.1*	2.8	*0.1*	8.5	*0.9*	3.1	*0.1*
	20	93.5	*0.1*	3	*0.1*	3.5	*0.9*	3.1	*0.1*
	21	91.8	*0.1*	2.9	*0.1*	5.3	*0.5*	3.1	*0.1*

Values in italic highlight the error

Table 3 ToF-ND alloy composition results. Average content (wt%)

Average concentration (wt%)						
Statuette section	Sn (wt%)	St. dev	Pb (wt%)	St. dev	Sn (wt%) Binary	St. dev
Shiva figurine	3.0	*0.2*	6.7	*2.3*	3.2	*0.2*
Pedestal (square)	2.7	*0.2*	3.3	*0.4*	2.8	*0.2*
Pedestal (lotus)	2.7	*0.2*	3.3	*0.6*	2.8	*0.2*
Halo	4.2	*0.1*	9.1	*2.0*	4.6	*0.1*

Values in italic highlight the highlight the standard deviation

shown in Fig. 10C as a 'box' of the same volume. The result shows that the pendant is made of a mixture of Au and Ag with a mass ratio of 1/46 (from a manufacturing practical point of view, it can be considered silver).

The ToF-ND phase analysis of the pendant sample volume (point no. 8) is characterized by the presence of bronze phase (alpha 1) at 36.3 wt% and by a second major phase at 63.2 wt%. The presence of phase alpha 1 of the bronze is explained as the gauge volume used for the measurements was 5 mm × 2 mm × 2 mm and covered a volume that includes both the pendant and the surrounding bronze. In fact, phase alpha 1 has the same composition as the other points on the body of the Shiva figurine. The other phase is instead representative of the pendant and potentially, it is a mixture of Ag–Cu-Au. It is not possible to reach such a lattice parameter value considering an Ag-Au mixture, since the lowest lattice parameter of this alloy is 10% higher than the one obtained. It is then necessary to include copper in the alloy and, because the Ag/Au ratio derived from NAA is 46:1, the Au contribution can be considered negligible. Considering, then, the Ag–Cu alloy (Cu cannot be measured within the pendant using NAA data), it is possible to obtain the measured lattice parameter only by performing quenching within a mould (due to its small size, the casting of the pendant can be considered a spontaneous quenching) since, at equilibrium, the maximum copper value hosted in silver is much lower (max 3 at%) providing a higher lattice parameter value. The resulting composition as derived from Pearson (Pearson 1958) and references within is 95.02 wt% ± 0.02 and Cu 4.98 wt% ± 0.02 (confirming again as silver from a practical point of view).

Casting techniques

Tomography data analysis also allows some details about the manufacturing method of the artefact to be inferred.

WB-NT undoubtedly shows that the statue was made in three distinct castings, using the direct lost wax technique: the Shiva statuette was cast together with the round footplate under his feet, while the base and the halo were cast independently. We tried to verify the sprue positions suggested by the literature (Craddock 2015). According to the traditional South Indian statuette casting technique, the gate system is built in the wax model, at the back of the statue. The main sprues can be located between the shoulder blades or directly in the nape. The mould is then typically buried in a casting pit (Craddock 2015; Levy, et al. 2007). As far as the mould position of the Shiva figurine is concerned, based on distribution of the pores, it is probable that the legs were oriented upwards, with the round base lying underfoot as a feeder. This is compatible

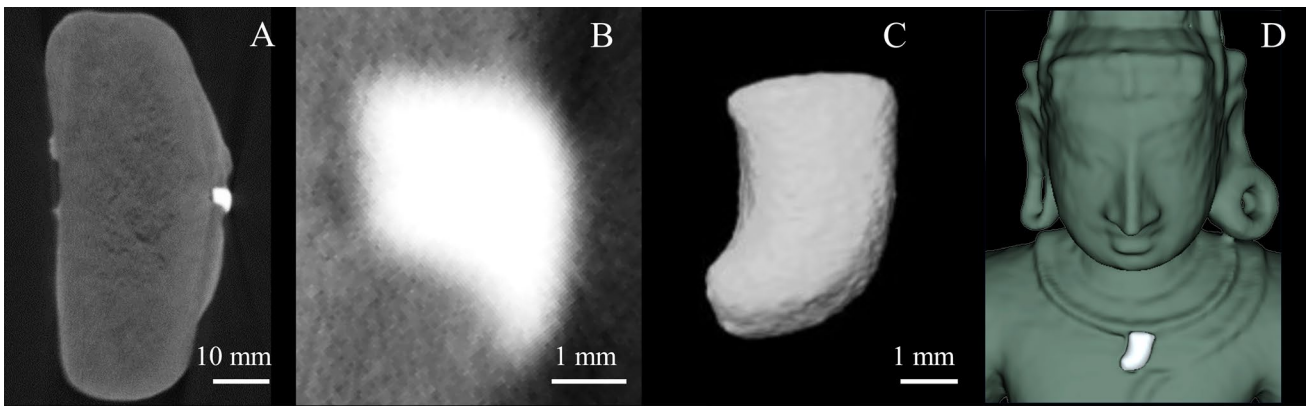

Fig. 10 **A** Axial slice of neutron tomography model of the Shiva's pendant from the FISH data. **B** Neutron tomography slice close-up detail. **C** 3D model of the Shiva's pendant as used for NAA quantitative composition correction and volume calculation. **D** Pendant position in the 3D volume reconstruction model

with the reconstructions proposed in the literature (Craddock 2015), showing a slightly tilted figurine, face down.

The analysis of the set of monochromatic radiographies in the wavelength range between $\lambda = 4.05$ Å and $\lambda = 4.20$ Å, crossing the (111) Bragg reflection of the Cu-Sn face-centered cubic alpha phase, shows the presence of anisotropic oligo-crystals (mm/sub-mm scale) which are constituted by single crystal grains oriented in different spatial directions. This phenomenon is present in the whole artefact: the Shiva figurine, the pedestal, and the halo (Fig. 11a–e) (see also Supplementary material S5 for full-size images). They appear as dark spots and the phenomenon is related to a strong coherent scattering effect removing neutrons from the primary beam. Oligo-crystals can certainly be attributed to the bronze microstructure since they are no longer visible in radiographs taken at wavelengths over the (111) family of copper lattice planes (FCC), where the scattering effect of such a phase contributes no more to the attenuation (Su, et al. 2021).

The uneven distribution of single crystal spots shown by ES-NR results for the halo (Fig. 12), together with neutron diffraction results (lead distribution (Fig S.21 in Supplementary material S6)) and related documentation of current production of bronze statuary in Tamil Nadu, allows us to formulate a hypothesis on the position of the halo mould during casting.

The presence of such oligo-crystals and dendrites suggests that the entire statuette has undergone a carefully controlled slow cooling. This is in agreement with the custom of placing the mould underground as is still done in the casting tradition of Tamil Nadu (Craddock & Hook 2007; Levy, et al. 2007).

Figure 13A shows that the presence of large-size crystallites interests the entire development of the halo, but their size abruptly decreases at the height of the left forearm. Moreover, it seems that the decrease of the crystals size appears to follow a certain angle. The size of the grains is inversely related to the speed of the solidification process; small crystals imply that part of the halo must have cooled down faster. Based on the models described in the literature, and on the traditional techniques used in contemporary South Indian workshops (Fig. 13B), a casting model for the halo is proposed (Fig. 13C): the mould was placed in the ground, tilted both towards the front (with the top of the arch pointing down), and sideways, with the left-side sprue only partially buried, thus exposing only that area of the mould to more rapid cooling.

Conclusions

This work demonstrates how non-invasive analysis can yield quantitative and qualitative physical properties of the interior of large solid cast bronzes. The investigation of the Shiva statuette (AK-MAK 1291) from the Rijksmuseum Asian Collection using different neutron-based techniques allowed us to inspect the bulk composition and

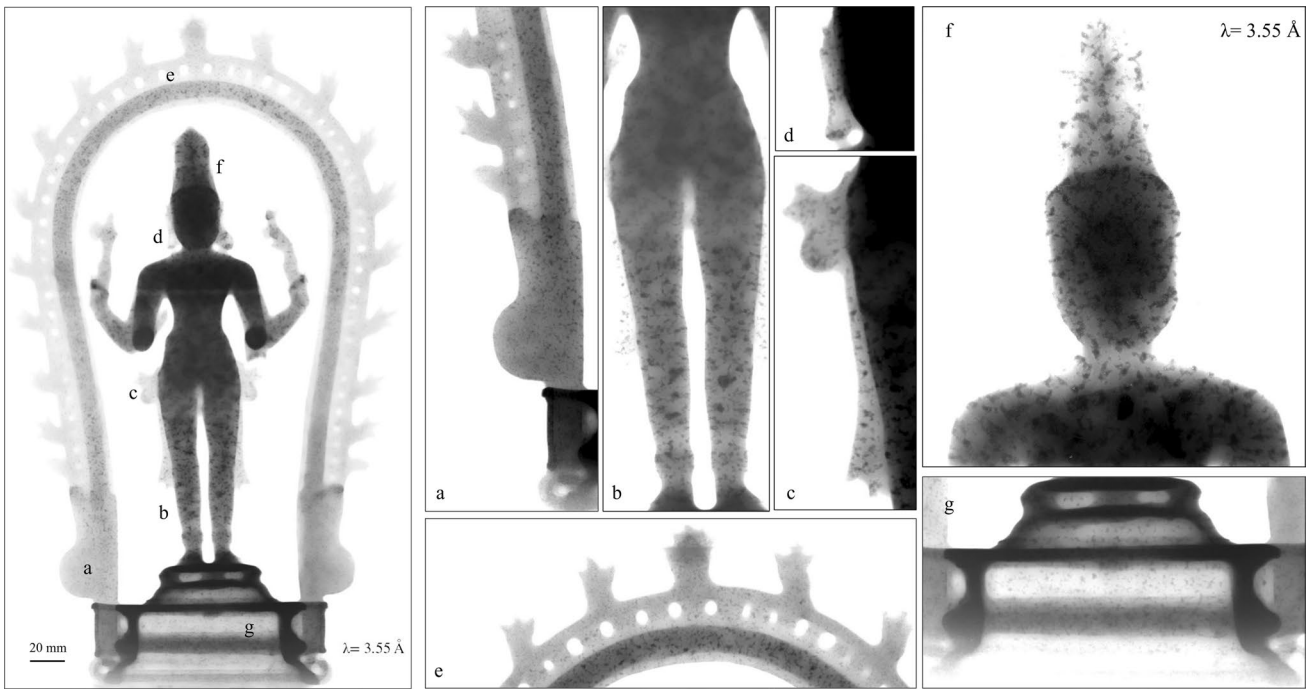

Fig. 11 Shiva (AK-MAK-1291)—selected monochromatic image at 3.55 Å neutron wavelength, obtained during energy-selective neutron radiography scan (for more details, see Supplementary material S5)

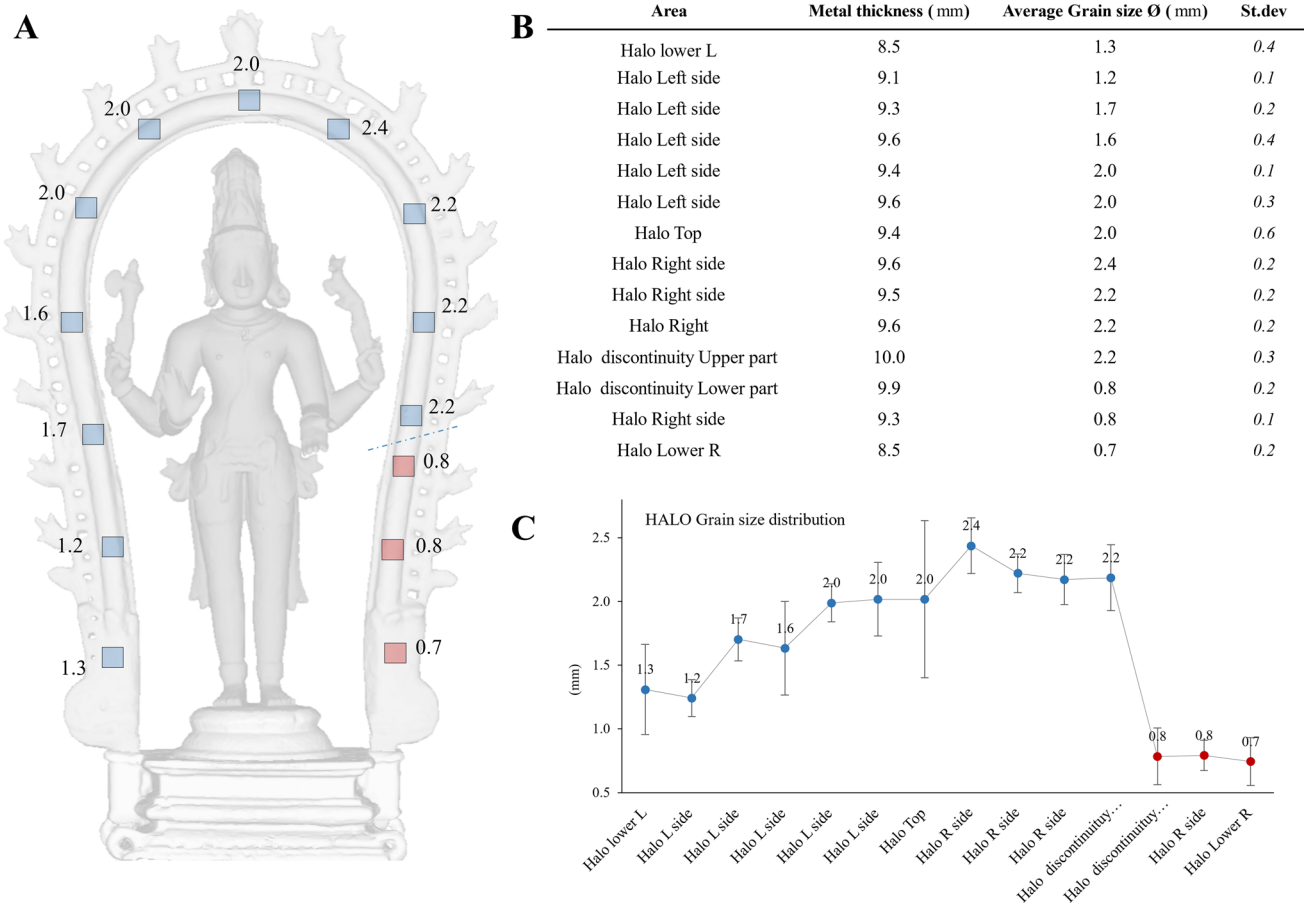

Area	Metal thickness (mm)	Average Grain size Ø (mm)	St.dev
Halo lower L	8.5	1.3	*0.4*
Halo Left side	9.1	1.2	*0.1*
Halo Left side	9.3	1.7	*0.2*
Halo Left side	9.6	1.6	*0.4*
Halo Left side	9.4	2.0	*0.1*
Halo Left side	9.6	2.0	*0.3*
Halo Top	9.4	2.0	*0.6*
Halo Right side	9.6	2.4	*0.2*
Halo Right side	9.5	2.2	*0.2*
Halo Right	9.6	2.2	*0.2*
Halo discontinuity Upper part	10.0	2.2	*0.3*
Halo discontinuity Lower part	9.9	0.8	*0.2*
Halo Right side	9.3	0.8	*0.1*
Halo Lower R	8.5	0.7	*0.2*

Fig. 12 Shiva (AK-MAK-1291)—oligo-crystal grain size. **A** Position of the 14 areas analysed on the halo. Within each area, the diameter of three grains was measured. In the table, **B** the average value of the oligo-crystal size is compared with the metal thickness of the relative section of the halo. **C** Halo grain size distribution in the different parts of the halo

conservation state and to reveal crucial details of manufacturing process. The ability to study the bulk of the statue, beyond the surface concretions and corrosion layers, allows investigation of the uncorroded bulk metal at length scales down to a few hundred micrometres.

Some of the main results concern the exploitation of the following:

- Local composition discrepancies which support hypotheses about casting techniques
- The presence of oligo-crystals in the body of the statue and in a large portion of the halo, suggesting the orientation of the mould and its cooling rate
- The presence and distribution of inner porosity to evaluate the orientation of the mould during the casting
- The identification of a special alloy used for the pendant inlay

Bronze artistic/archaeological artefacts fabricated by means of direct lost wax casting are unique and irreproducible objects. Therefore, even if this type of statuette has been studied from an archaeological and stylistic point of view, only a technological study of the individual artefact can shed light on the methods actually used to make it. In this work, it was possible to provide a morphological and microstructural characterization of the entire statuette, to describe the state of conservation of the bulk of the artefact, and to identify and quantify the main mineralization phases. Although it is a solid cast statue, the WB-NT allowed us to visualize fine several microstructural details, for instance, dendrites, which allow us to confirm that the Shiva figurine was cast as a whole with the flattened round plate under his feet. The morphological analysis through the study of the axial, sagittal, and normal tomographic stacks, also exploiting non-orthogonal reslicing, allowed us to obtain information on the assembly of the pedestal. Furthermore, the quantitative analysis of the bronze alloy was obtained by means of ToF-ND: by combining the results of the WB-NT, NAA, and ToF-ND, the composition of the pendant of the necklace was also obtained.

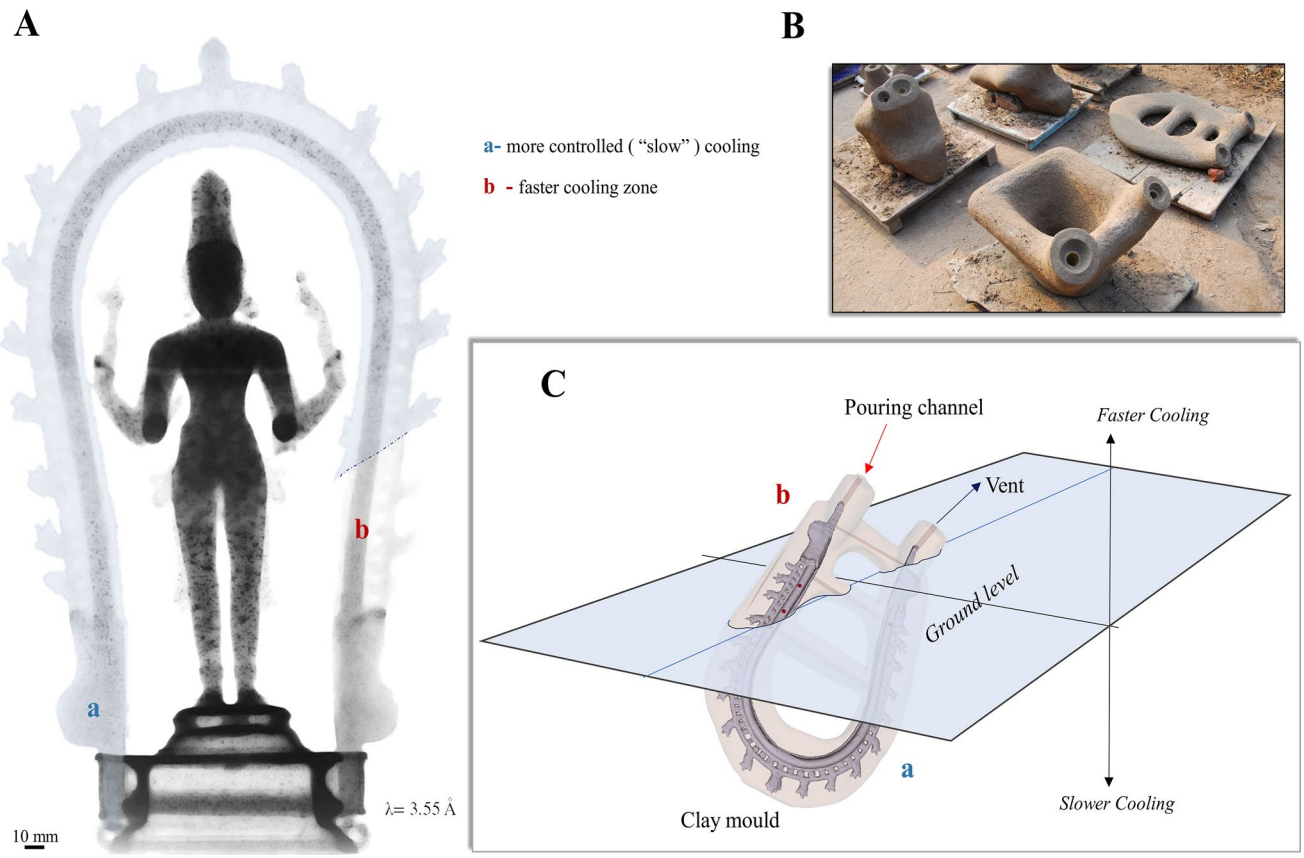

Fig. 13 Shiva (AK-MAK-1291)—hypothesis of positioning of the mould for casting the 'halo': **A** in blue, the 'Halo' area probably subjected to slower cooling; **B** clay moulds for decorative elements left to dry in a traditional Tamil Nadu artisan 'workshop' (*credit courtesy of Rijksmuseum*); **C** diagram of a possible arrangement of the mould in the ground. The mould was likely inclined with the top of the arch facing downwards (a) and rotated with one of the sprues raised above ground level so as to expose a small part of the halo (b) to fast cooling

Moreover, some clues concerning the casting method were obtained; for example, the ES-NR scan showed the presence in the structure of grain oligo-crystals. The size and ubiquitous distribution of these single crystals would not have been possible without careful cooling of the mould after casting. The cooling must have been slow enough to allow these crystals to grow to millimetre-scale size. Furthermore, the abrupt decrease in the size of the grains on the left side of the halo allowed us to propose a reconstruction of the position of the mould during casting. It is important to underline that all results were obtained in a completely non-invasive way.

Supplementary Information The online version contains supplementary material available at https://doi.org/10.1007/s12520-024-01948-z.

Author contribution F.G., F. C., and S.C.: conceptualization; F.C.: original draft writing and figure preparation; N.K., F.C., F.G., and S.C.: WB-NT and ESNI data acquisition (at HZB); L.v.E., Y.L., and S. C.: WB-NT and NAA data acquisition (at TU-Delft); S. K., F.C., F.G., and S.C.: ToF-ND data acquisition (at ISIS); F.C. and F.G.: WB-NT and ESNI data curation; Y.L. and L.v.E.: NAA data curation; F.G. and F.C.: ToF-ND data curation; F.C., F.G., L.v.E., Y.L., and S.C.: editing. All authors reviewed the manuscript.

Data Availability The data presented in this study are available on request from the corresponding author.

Declarations

Competing interests None of the authors have competing interests as defined by Springer, or other interests that could be perceived as influencing the findings and/or discussion reported in this article.

References

Azéma A, Chauveau D, Porot G, Angelini F, Mille B (2017) Pour une meilleure compréhension du procédé de soudage de la grande statuaire antique en bronze: analyses et modélisation expérimentale. *Technè. La science au service de l'histoire de l'art et de la préservation des biens culturels* 45:73–83

Cantini F et al (2023) The Vittoria Alata from Brescia: a combined neutron techniques and SEM-EDS approach to the study of the alloy of a bronze Roman statue. J Archaeol Sci Rep 51(104112):1–17
Craddock PT (2015) The metal casting traditions of South Asia: continuity and innovation. Indian J Hist Sci 1(50):55–82
Craddock P, Hook D (2007) The bronze industries of South India: a continuing tradition? Freer Gallery of Art, Washington DC
Dehejia V (2021) The thief who stole my heart: the material life of sacred bronzes from Chola India. Princeton University Press, s.l.
Dierick M, Masschaele B, Van Hoorebeke L (2004) Octopus, a fast and user-friendly tomographic reconstruction package developed in LabView®. Meas Sci Technol 15(3):1366–1371
Fedorov A et al (2012) 3D Slicer as an image computing platform for the quantitative imaging network. Magn Reson Imaging 30(9):1323–1341
Giumlia-Mair A (2012) The technology of bronze statuary. In Myth, allegory, emblem: the many lives of the Chimaera of Arezzo. Malibu, Aracne, pp 167–184
Grazzi F, Bartoli L, Siano S, Zoppi M (2010) Characterization of copper alloys of archaeometallurgical interest using neutron diffraction: a systematic calibration study. Anal Bioanal Chem 397:2501–2511
Grazzi F et al (2018) The investigation of Indian and central Asian swords through neutron methods. J Archaeol Sci Rep 20:834–842
Greenberg RR, Bode P, De Nadai Fernandes EA (2011) Neutron activation analysis: a primary method of measurement. Spectrochim Acta, Part B 66(3–4):193–241
Hughes MJ, Northover JP, Staniaszek BEP (1982) Problems in the analysis of leaded bronze alloys in ancient artefacts. Oxf J Archaeol 1:359–364
Josic L, Lehmann E, Kaestner A (2011) Energy selective neutron imaging in solid state materials science. Nucl Instrum Methods Phys Res, Sect A 1(651):166–170
Kardjilov N, Hilger A, Manke I, Banhart J (2014) The neutron imaging instrument at HZB. Neutron News 25(2):23–26
Lehmann EH, Deschler-Erb E, Ford A (2010) Neutron tomography as a valuable tool for the non-destructive analysis of historical bronze sculptures. Archaeometry 52(2):272–285
Levy T, Levy A, Sthapathy DR (2007) Master of fire -hereditary bronze caster of South India. Deutsches Bergbau-Museum, Bochum
Oudbashi O et al (2020) Arsenical copper and bronze metallurgy during Late Bronze Age of north-eastern Iran: evidences from Shahrak-e Firouzeh archaeological site. Archaeol Anthropol Sci 12:1–20
Pearson WB (1958) A handbook of lattice spacings and structures of metals and alloys. Pergamon Press, Oxford
Rasband WS (2007) ImageJ, US national institutes of health. http://rsb.info.nih.gov/ij/ (1997-2007)
Rueden CT, Schindelin J, Hiner MC, DeZonia BE, Walter AE, Arena ET, Eliceiri KW (2017) ImageJ2: ImageJ for the next generation of scientific image data. BMC Bioinform 18:1–26
Salvemini F et al (2023) An insight into a Shang dynasty bronze vessel by nuclear techniques. Appl Sci 13(3):1549
Salvemini F, Grazzi F, Peetermans S, Civita F, Franci R, Hartmann S, Lehmann E, Zoppi M (2012) Quantitative characterization of Japanese ancient swords through energy-resolved neutron imaging. J Anal At Spectrom 27(9):1494–1501
Schulz M, Lehmann E, Losko A (2024) Neutron imaging. In: Non-Destructive Material Characterization Methods. Elsevier, pp 205–247
Scott DA (1991) Metallography and microstructure of ancient and historic metals. s.l.:Getty Conservation Centre, Los Angeles
Slaczka A, Creange S, Van Bennekom J (2019) Nataraja informed through text and technique: a study of the monumental indian bronze at the Rijksmuseum. Rijksmus Bull 67(1):5–29
Srinivasan S (2006) The art and science of Chola bronzes. Orientations 37(8):46–54
Srinivasan S (1999) Preliminary insights into the provenance of South Indian copper alloys and images using a holistic approach of comparisons of their lead isotopes and chemical composition with slags and ores. Archaeopress, 200–210
Su Y, Oikawa K, Shinohara T (2021) Neutron Bragg-edge transmission imaging for microstructure and residual strain in induction hardened gears. Sci Rep 11(1):4155
Toby BH (2001) EXPGUI, a graphical user interface for GSAS. J Appl Crystallogr 34:210–213
van Well AA, De Haan VO, Rekveldt MT (1991) Stacked neutron guides at IRI Delft. Neutron News 3(2):28
Von Dreele RB, Larson AC (2004) General structure analysis system (GSAS). Los Alamos Natl Lab Rep LAUR 748:86–748
Werner O (1972) Spektralanalytische und metallurgische Untersuchungen an indischen Bronzen. Brill, Leiden
Zhou Z et al (2018) FISH: a thermal neutron imaging station at HOR Delft. J Archaeol Sci Rep 20:369–373